Analytical and numerical evaluation of electron-injection detector optimized for SWIR photon detection

Yashar Movassaghi, Vala Fathipour, Morteza Fathipour, and Hooman Mohseni

---

Analytical and numerical evaluation of electron-injection detector optimized for SWIR photon detection

Yashar Movassaghi,[1,a)] Vala Fathipour,[2,a)] Morteza Fathipour,[1] and Hooman Mohseni[2]

[1]*Modeling and Simulation of Semiconductor Devices Laboratory, Department of Electrical and Computer Engineering, University of Tehran, Tehran, Iran*
[2]*Bio-Inspired Sensors and Optoelectronics Laboratory, Northwestern University, 2145 Sheridan Rd, Evanston, Illinois 60208, USA*

Recent results from our electron-injection detectors as well as other heterojunction phototransistors with gain suggest that these devices are useful in many applications including medical imaging, light detection and ranging, and low-light level imaging. However, there are many parameters to optimize such structures. Earlier, we showed a good agreement between experimental results and our models. In this paper, we provide detailed analytical models for rise time, gain, and dark current that very accurately evaluate key parameters of the device. These show an excellent agreement with detailed three-dimensional numerical simulations. We also explore a figure of merit that is useful for low-light-detection applications. Based on this figure of merit, we examine the ultimate sensitivity of the device. Furthermore, we explore the effects of variations in some of the key parameters in the device design and present an optimum structure for the best figure of merit. Our models suggest ways to improve the existing devices that we have, and may be a guideline for similar phototransistors. *Published by AIP Publishing.* [http://dx.doi.org/10.1063/1.4976012]

I. INTRODUCTION

The short wavelength infrared (SWIR) band (from 1 to 2.5 μm) has a variety of diverse applications. These include telecommunication, remote sensing, astronomical observation, medical imaging, homeland security, and non-destructive material evaluation.[1–3] As such, significant amount of research has been devoted to the development of sensitive SWIR detectors with low noise levels and high signal-to-noise ratios. State-of-the-art semiconductor SWIR detectors include p-i-n detectors and avalanche photo detectors (APDs). InGaAs p-i-n detectors have extremely low leakage current levels and short response times. Unfortunately, due to the lack of internal amplification in such detectors, the system signal-to-noise ratio becomes mostly limited by the electrical noise of the post-detection circuitry.[4] Detectors with an internal gain mechanism, such as avalanche photodiodes offer an overall system-level sensitivity enhancement compared to p-i-n diodes.[5] InGaAs/InP APDs provide stable gain values close to 3 at ∼25 V at room temperature.[6] Unfortunately, due to the internal positive feedback in the avalanche multiplication process, their gain tends to destabilize at higher values and increase the amplitude uncertainty.[7] As such they suffer from an excess noise factor, and have a large gain sensitivity to the bias voltages.

With the growing applications for more sensitive SWIR detectors, the demand for new SWIR photodetector technologies has become more urgent than ever. Electron–injection (EI) detectors are based on a new photon-detection approach in the SWIR band and can address these shortcomings. They operate in the linear-mode and at low bias voltages.[8] These detectors provide a high avalanche-free amplification, unity

excess noise, and low leakage current.[9–12] Experimental results have shown that devices with 10 μm injector diameter and 30 μm absorber diameter provide a peak optical gain of more than ∼1000, dark current ∼15 nA, and a fast rise time of ∼10 ns at 20 μW of optical power at a bias voltage of ∼−3 V and room temperature.[13] An essential tool for further understanding and improvement of this detector is the existence of compact, physics based analytical models. We have previously presented the analytical models and have confirmed those models by simulations and experimental measurement data.[15] In this paper, we intend to present a detailed derivation of the analytical models for the detector speed, dark current and also to elaborate on our gain model. Furthermore, we present the results on the global optimization of the device using a figure of merit (FOM) that is useful especially in low-light-level detection. Using these data, one can optimize the EI detector or other devices of similar nature, and examine the ultimate physical sensitivity of the device. The simulation software package used for this work is a commercial device simulator (ATLAS from Silvaco International). The numerical simulation of the electron-injection detector has been carried out assuming that semiconductor is non-degenerate and has parabolic conduction bands. The simulation involves the solution of five coupled equations using Newton's iteration algorithm. Fermi-Dirac statistics were used in the calculation of the carrier concentrations. Generation-recombination mechanisms were approximated by concentration dependent Shockley–Read–Hall (SRH) as well as radiative (the optical Band to Band) and Auger models. Furthermore, other effects including incomplete ionization, surface recombination, concentration dependent mobility, band gap narrowing, and hot electron effects were employed in the simulation. In Section II of this paper, we present

---

a)Y. Movassaghi and V. Fathipour contributed equally to this work.

derivations for the analytical models. In Section III, we provide results of our global optimization, and finally in Section IV, we provide a conclusion.

II. DERIVATION FOR THE ANALYTICAL MODELS

The structure under consideration consists of 500 nm of n^+ ($10^{17} cm^{-3}$) InP injector, 50 nm of undoped $In_{0.52}Al_{0.48}As$ etch-stop, 50 nm of p^+ ($5.0 \times 10^{18} cm^{-3}$) $GaAs_{0.52}Sb_{0.48}$ trapping layer, 1000 nm of n^- ($<1 \times 10^{15} cm^{-3}$) $In_{0.53}Ga_{0.47}As$ absorber. Layers are grown on InP substrate using metal organic chemical vapor deposition (MOCVD). A schematic of the detector structure with 10 μm injector diameter and 30 μm absorber is shown in Fig. 1(a). Energy band diagrams along the central axis of the device obtained by ATLAS are shown in Fig. 1(b). A schematic cross-sectional view of the device
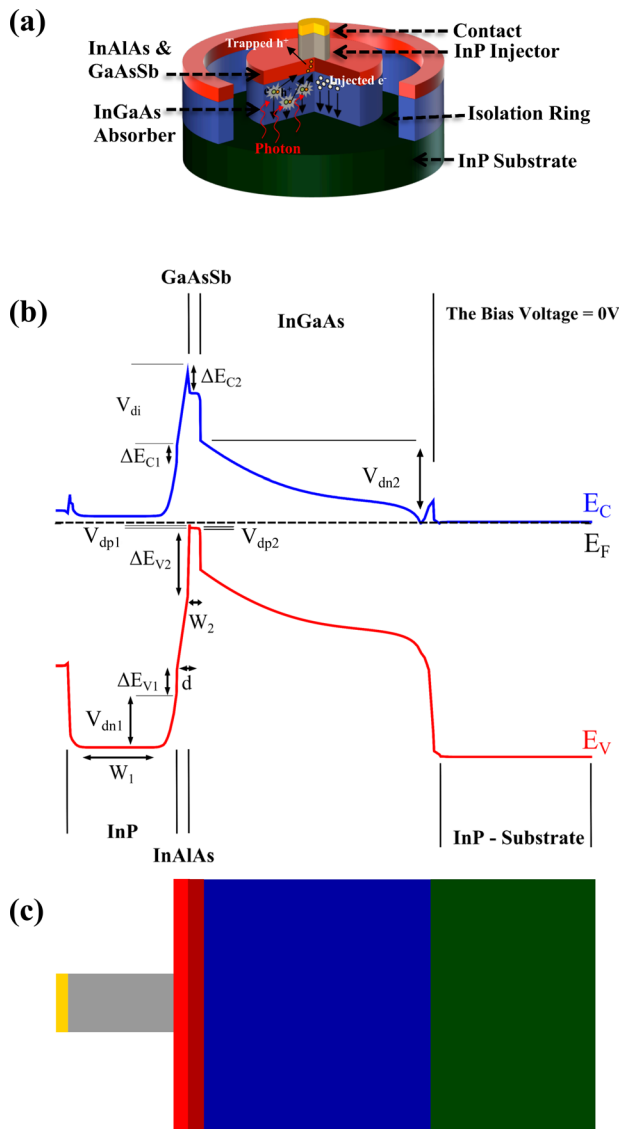
that is equal in width to the equilibrium energy band diagram is shown in Fig. 1(c).

A. Dark current

In Fig. 1, the energy offsets form in the conduction band (ΔE_C) and in the valence band (ΔE_V) as a result of differences in gradients in the electrostatic potential (ΔV) and the electron affinity ($\Delta \chi$). The conduction and valence band–edge discontinuities at the heterointerfaces (dependent on $E_{gn}, E_{gp}, N_A, N_D, \chi$), and the built-in potentials V_{d1} and V_{d2} after formation of the heterojunctions are related as

$$\Delta E_C = \Delta E_{C_{1,2}} + \Delta E_{C_{2,3}}, \tag{1}$$

$$\Delta E_V = \Delta E_{V_{1,2}} + \Delta E_{V_{2,3}}, \tag{2}$$

$$V_d = V_{dn1} + V_{di} + V_{dp1}. \tag{3}$$

Here, V_d is the total built-in potential, and V_{dn1}, V_{dp1}, and V_{di} are the barriers corresponding to band bending on the n^+-InP, p^+-GaAsSb and on the undoped InAlAs sides. The current flowing through the detector has two major components:

1. The diffusion current arising from the minority carriers injected to the p^+—GaAsSb region and the n^+—InP region.
2. The current arising from generation recombination (GR) in the depletion regions of the InP/InAlAs/GaAsSb junctions and InGaAs/GaAsSb junction. This current is typically dominant in transistors built from compound semiconductor materials.[19]

The device is designed to normally operate under forward bias. When a positive voltage is applied to the injector layer, the InP/GaAsSb junction becomes reverse biased. The dark current is then limited by drift current. On the other hand, when a negative voltage is applied to the InP/GaAsSb junction, this junction becomes forward bias. Under this condition, electrons acquire enough energy to get injected from InP into the InGaAs absorber. For more negative bias voltages, i.e., $V_{bias} < -0.5$ V, the voltage drop on the InP/GaAsSb becomes relatively constant and as a result, the current increases sub-linearly with respect to the bias voltage. This current is dominated by the thermal generation of electron-hole pairs within the depletion region. To derive the dark current, we use a similar approach as in Ref. 16. The steady-state continuity equations governing the distribution of minority carriers in the GaAsSb are given by

$$D_n \frac{\partial^2 \delta n(x)}{\partial x^2} = \frac{\delta n}{\tau_n}, \quad 0 < x < W_2. \tag{4}$$

Furthermore, in the InP region, distribution of minority carriers is given by

$$D_p \frac{\partial^2 \delta p(x)}{\partial x^2} = \frac{\delta p}{\tau_p}, \quad 0 < x < W_1, \tag{5}$$

where τ_n (τ_p) are lifetimes for minority carrier electrons (holes), respectively, in p^+—GaAsSb (n^+—InP). δn (δp) are the excess electron (hole) density, respectively, in the GaAsSb (InP) regions. W_1 is the width of undepleted InP

FIG. 1. (a) Schematic diagram of the electron-injection detector.[15] Reproduced with permission from Appl. Phys. Lett. **108**, 121102 (2016). Copyright 2016 AIP Publishing LLC. (b) The equilibrium energy band diagram of an electron-injection detector along a cutline through the central axis of the device generated using ATLAS software, in darkness. (c) A schematic cross-sectional view of the device that is equal in width to the equilibrium energy band diagram shown in (b).

injector layer, and W_2 is the width of undepleted GaAsSb trapping layer. Excess electron and hole densities in the GaAsSb and InP regions are obtained by analytically solving the continuity equations under appropriate boundary conditions. Assume that the device is operating under normal operating conditions, i.e., GaAsSb/ InGaAs junction is reverse biased, and the InP/GaAsSb junction is forward biased, the results are given below

$$\delta n(x) = \frac{\Delta n_p \left[\cosh\left(\frac{W_2 - x}{L_n}\right) + \frac{S_n L_n}{D_n} \sinh\left(\frac{W_2 - x}{L_n}\right) \right]}{\cosh\left(\frac{W_2}{L_n}\right) + \frac{S_n L_n}{D_n} \sinh\left(\frac{W_2}{L_n}\right)}, \quad (6)$$

$$\delta p(x) = \frac{\Delta p_n \left[\cosh\left(\frac{W_1 - x}{L_p}\right) + \frac{S_p L_p}{D_p} \sinh\left(\frac{W_1 - x}{L_p}\right) \right]}{\cosh\left(\frac{W_1}{L_p}\right) + \frac{S_p L_p}{D_p} \sinh\left(\frac{W_1}{L_p}\right)}, \quad (7)$$

where L_n and L_p are the electrons and hole diffusion lengths, respectively. D_n and D_p are diffusion coefficients for the electrons and holes on p^+ and n^+ sides, S_n and S_p are the surface recombination velocities for electrons and holes at the interfaces, and Δp_n and Δn_p are excess hole concentration at the edge of (InP) injector depletion region and excess electron concentration at the edge of (GaAsSb) trapping layer depletion region, respectively. The standard one-dimensional diffusion equation for the heterojunction under consideration has been solved to obtain the expression for the diffusion current in the p^+ GaAsSb and n^+ InP active regions. The diffusion current for electrons and holes is given by

$$I_{sn} = q A_1 D_n \left. \frac{\partial \delta n(x)}{\partial x} \right|_{x=0}$$

$$= \frac{q A_1 n_{ip}^2}{N_A} \sqrt{\frac{\mu_n k_B T}{q \tau_n}} \frac{\left[\sinh\left(\frac{W_2}{L_n}\right) + \frac{S_n L_n}{D_n} \cosh\left(\frac{W_2}{L_n}\right) \right]}{\cosh\left(\frac{W_2}{L_n}\right) + \frac{S_n L_n}{D_n} \sinh\left(\frac{W_2}{L_n}\right)}$$

$$\times \exp\left(\frac{-q(V_d + \Delta E_C)}{k_B T}\right), \quad (8)$$

$$I_{sp} = q A_1 D_p \left. \frac{\partial \delta p(x)}{\partial x} \right|_{x=0}$$

$$= \frac{q A_1 n_{in1}^2}{N_D} \sqrt{\frac{\mu_p k_B T}{q \tau_p}} \frac{\left[\sinh\left(\frac{W_1}{L_p}\right) + \frac{S_p L_p}{D_p} \cosh\left(\frac{W_1}{L_p}\right) \right]}{\cosh\left(\frac{W_1}{L_p}\right) + \frac{S_p L_p}{D_p} \sinh\left(\frac{W_1}{L_p}\right)}$$

$$\times \exp\left(\frac{-q(V_d + \Delta E_V)}{k_B T}\right). \quad (9)$$

In (8) and (9), n_{in1} and n_{ip} are the intrinsic carrier concentrations, calculated from the corresponding band gaps (E_g) and effective density of states in conduction and valence bands (N_c and N_V), provided in Table I, and N_D and N_A are the donor and acceptor concentrations in the n^+ InP and p^+ GaAsSb regions respectively. A_1 is the injector area, q is the electron charge, k_B is the Boltzmann constant, T is the

temperature, and μ_n and μ_p are the electron and hole mobilities. The total diffusion current can be expressed as

$$I_{DIFF} = (I_{sn} + I_{sp}) \left(\exp\left(\frac{q V_{BE}}{k_B T}\right) - 1 \right). \quad (10)$$

Simulation results indicate that inclusion of the radiative generation/recombination in the models does not affect the results. Radiative recombination rate in the electron-injection detector is intrinsic to the bulk material, while the Shockley-Read-Hall (SRH) recombination life times are heavily material quality and processing dependent. With the material properties and device geometry, we have, (i.e., the large surface to volume ratio) the SRH channel appears to be much faster, and thus, the effect of radiative recombination is negligible. As such, the carrier generation-recombination in the depletion regions is modeled by the SRH equation. For simplicity, we assume that the electrons and holes lifetimes due to Shockley-Read-Hall recombination are equal and can be modeled as

$$\tau_{SRH} = \frac{1}{\sigma N_f v_{th}}, \quad (11)$$

where N_f is the SRH trap density, σ is the capture cross-section, and v_{th} is the thermal carrier velocity given by

$$v_{th} = \sqrt{\frac{3 k_B T}{m^*}}. \quad (12)$$

In (12), m^* is the effective mass of the charge carriers. The generation recombination current in the depletion regions can be obtained as

$$I_{GR} = I_{GR}^{01} \exp\left(\frac{q V_{BE}}{2 k_B T}\right) + I_{GR}^{02} \exp\left(\frac{q V_{BC}}{2 k_B T}\right), \quad (13)$$

where $I_{GR}^0 = \frac{2 A k_B T n_i \sigma N_f}{E} \sqrt{\frac{3 k_B T}{m^*}}$ is the generation-recombination current at zero applied bias (equilibrium condition), and E is the electric field in the depletion region. Under an equilibrium condition, the generation-recombination current is given by

$$I_{GR}^{01} = \frac{2 A_1 k_B T n_{in1} \sigma N_f x_n}{V_{dn1}} \sqrt{\frac{3 k_B T}{m_{nn1}^*}} + \frac{2 A_2 k_B T n_i \sigma N_f d}{V_{di}}$$

$$\times \sqrt{\frac{3 k_B T}{m_{n0}^*}} + \frac{2 A_2 k_B T n_{ip} \sigma N_f x_{p1}}{V_{dp1}} \sqrt{\frac{3 k_B T}{m_{pp}^*}}, \quad (14)$$

$$I_{GR}^{02} = \frac{2 A_2 k_B T n_{in2} \sigma N_f d_n}{V_{dn2}} \sqrt{\frac{3 k_B T}{m_{nn2}^*}} + \frac{2 A_2 k_B T n_{ip} \sigma N_f x_{p2}}{V_{dp2}} \sqrt{\frac{3 k_B T}{m_{pp}^*}}, \quad (15)$$

where V_{dn2} and V_{dp2} are the barriers corresponding to band bending on the n-InGaAs, p^+-GaAsSb sides as shown in Fig. 1. In (16), x_n is the width of depletion region in the InP injector, and x_{p1}, and x_{p2} are depletion widths in the GaAsSb layer at the interface with InAlAs and InGaAs, respectively, d and d_n are the InAlAs and InGaAs depletion thicknesses, m_{nn1}^*, m_{n0}^*, m_{pp}^* and m_{nn2}^* are the effective masses of electrons and

TABLE I. Parameters used in the analytical model for dark current at room temperature.

Parameter	Symbol	Values	References
Capture cross-section of minority carriers	σ	2×10^{-17} cm^2	16 and 22
Shockley Read Hall trap density	N_f	1×10^{15} cm^{-3}	16 and 22
Width of undepleted InP injector	W_1	0.318×10^{-4} cm	Extracted from band diagram
Width of undepleted GaAsSb trap layer	W_2	0.032×10^{-4} cm	Extracted from band diagram
Width of undepleted InGaAs absorption layer	W_3	0.004×10^{-4} cm	Extracted from band diagram
Electron diffusion coefficient of InP	D_n	130 cm^2/s	16, 23, 24, and 25
Hole diffusion coefficient of GaAsSb	D_p	10 cm^2/s	16, 23, 24, and 25
Electron surface recombination velocity	S_n	10^4 cm/s	16, 23, and 24
Hole surface recombination velocity	S_p	10^2 cm/s	16, 23, and 24
Width of depleted InP injector layer	x_n	0.077×10^{-4} cm	Extracted from band diagram
Width of depleted GaAsSb trap layer (at the edge of InAlAs heterojunction)	x_{p1}	0.01202×10^{-4} cm	Extracted from band diagram
Width of depleted GaAsSb trap layer (at the edge of InGaAs heterojunction)	x_{p2}	0.01202×10^{-4} cm	Extracted from band diagram
Barrier corresponding to band bending on the InP	V_{dn1}	0.10347 eV	Extracted from band diagram
Barrier corresponding to band bending on the InAlAs	V_{di}	0.27102 eV	Extracted from band diagram
Barrier corresponding to band bending on the GaAsSb	V_{dp1}	0.002341 eV	Extracted from band diagram
Barrier corresponding to band bending on the GaAsSb	V_{dp2}	0.04 eV	Extracted from band diagram
Barrier corresponding to band bending on the InGaAs	V_{dn2}	0.48459 eV	Extracted from band diagram
Electron effective density of state for InP	N_{C1}	5.4×10^{17} cm^{-3}	15, 16, 23, and 24
Hole effective density of state for InP	N_{V1}	1.3×10^{19} cm^{-3}	15, 16, 23, and 24
Electron effective density of state for InAlAs	N_{C2}	5.2×10^{17} cm^{-3}	15, 16, 23, and 24
Hole effective density of state for InAlAs	N_{V2}	1.2×10^{19} cm^{-3}	15, 16, 23, and 24
Electron effective density of state for GaAsSb	N_{C3}	2.4×10^{17} cm^{-3}	15, 16, 23, and 24
–Hole effective density of state for GaAsSb	N_{V3}	7.5×10^{18} cm^{-3}	15, 16, 23, and 24
Electron effective density of state for InGaAs	N_{C4}	2.1×10^{17} cm^{-3}	15, 16, 23, and 24
Hole effective density of state for InGaAs	N_{V4}	8.9×10^{18} cm^{-3}	15, 16, 23, and 24
Energy gap for InP	E_{g1}	1.35 eV	15, 16, 23, and 24
Energy gap for InAlAs	E_{g2}	1.3107 eV	15, 16, 23, and 24
Energy gap for GaAsSb	E_{g3}	0.787 eV	15, 16, 23, and 24
Energy gap for InGaAs	E_{g4}	0.754 eV	15, 16, 23, and 24
Conduction band-edge discontinuity in the InP/InAlAs	$\Delta E_{C1,2}$	0.1 eV	16, 23, and 24
Conduction band-edge discontinuity in the InAlAs/GaAsSb	$\Delta E_{C2,3}$	0.105 eV	16, 23, and 24
Valence band-edge discontinuity in the InP/InAlAs	$\Delta E_{V1,2}$	0.140 eV	16, 23, and 24
Valence band-edge discontinuity in the InAlAs/GaAsSb	$\Delta E_{V2,3}$	0.427 eV	16, 23, and 24
Conduction band-edge discontinuity in the InGaAs/GaAsSb	$\Delta E_{C3,4}$	0.234 eV	16, 23, and 24
Valence band-edge discontinuity in the InGaAs/GaAsSb	$\Delta E_{V3,4}$	0.2 eV	16, 23, and 24
Electron effective mass in InP	m^*_{nn1}/m_0	0.077	23 and 24
Electron effective mass in InAlAs	m^*_{n0}/m_0	0.075	23 and 24
Hole effective mass in GaAsSb	m^*_{pp}/m_0	0.456	23 and 24
Electron effective mass in InGaAs	m^*_{nn2}/m_0	0.044	23 and 24

holes in the InP and InAlAs and GaAsSb and InGaAs regions, respectively. A_2 is the absorber area. The details of parameters used in the derivation of the dark current analytical models are reported in Table I.

Using Equations (14) and (15), the generation-recombination current can be expressed as

$$I_{GR} = 2\sqrt{3(k_B T)^3}\,\sigma N_f \left[\frac{A_1 n_{in1} x_n}{V_{dn1}} \sqrt{\frac{1}{m^*_{nn1}}} + \frac{A_2 n_i d}{V_{di}} \sqrt{\frac{1}{m^*_{n0}}} \right.$$
$$\left. + \frac{A_2 n_{ip} x_{p1}}{V_{dp1}} \sqrt{\frac{1}{m^*_{pp}}} \right] \exp\left(\frac{qV_{BE}}{2k_B T}\right) + 2\sqrt{3(k_B T)^3}\,\sigma N_f$$
$$\times \left[\frac{A_2 n_{in2} d_n}{V_{dn2}} \sqrt{\frac{1}{m^*_{nn2}}} + \frac{A_2 n_{ip} x_{p2}}{V_{dp2}} \sqrt{\frac{1}{m^*_{pp}}} \right] \exp\left(\frac{qV_{BC}}{2k_B T}\right).$$

(16)

Potential profile at 4 different bias voltages along a cutline through the central axis of the device is shown in Fig. 2(a). Evolution of V_{BE} and V_{BC} for the injector–trapping layer (InP/InAlAs/GaAsSb) and trapping layer–absorber (GaAsSb/InGaAs) junctions versus bias voltage is plotted in the inset of Figure 2(a). Recombination in the GaAsSb/InGaAs space-charge-region relative to InP/InAlAs/GaAsSb charge region dominates as the magnitude of the bias voltage decreases, and InP/InAlAs/GaAsSb recombination current dominates for bias voltages larger than $\sim|0.3\,\text{V}|$. Fig. 2(c) shows the diffusion and GR terms for the dark current and indicates that dark current is limited by the GR component. Fig. 2(d) shows a comparison of the experimental data, obtained from Ref. 15, with numerical and analytical models for the electron-injection detector dark current with 10 μm injector and 30 μm absorber diameter. Finally, we have obtained the Arrhenius plot for the detector dark current versus 1000/
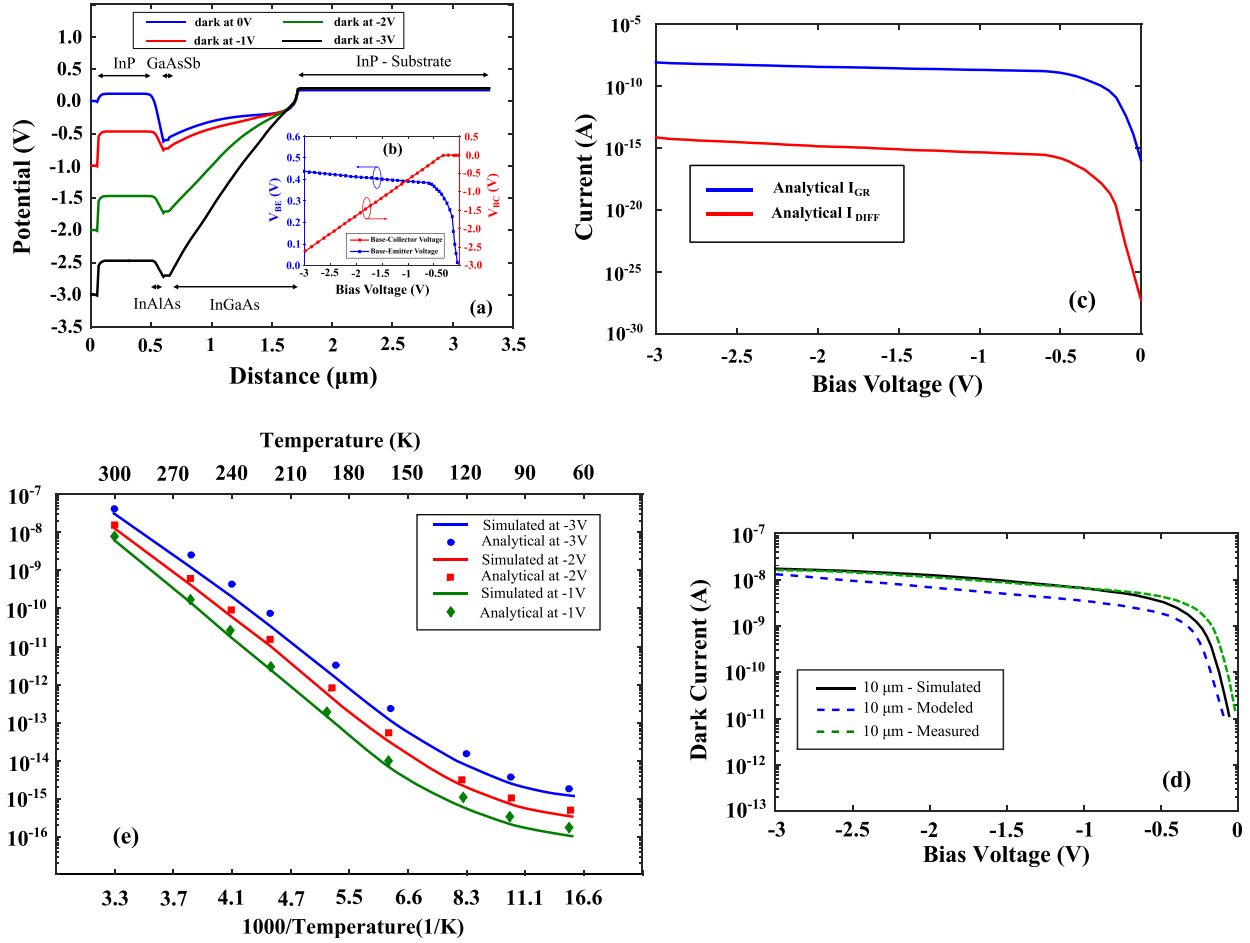
FIG. 2. (a) potential profile along a cutline through the central axis of the device. (b) Evolution of V_{BE} and V_{BC} with the applied bias voltage (V). (c) Dark current components versus bias voltage. (d) A comparison of the experimental data with numerical and analytical models for electron-injection detector with 10 μm injector and 30 μm absorber diameter.[15] Reproduced with permission from Appl. Phys. Lett. **108**, 121102 (2016). Copyright 2016 AIP Publishing LLC. (e) The Arrhenius plot of the dark current versus temperature for electron-injection detector with 10 μm injector and 30 μm absorber diameter at a different bias voltage.

temperature at different bias voltages. As the temperature reduces, the generation–recombination in the InGaAs/GaAsSb junction and in the InP/InAlAs/GaAsSb junction also reduce. The extracted activation energy from Fig. 2(e) confirms the G-R dominated dark current behavior. The Arrhenius plot shows a slight curvature due to $T^{3/2}$ term. Finally the dark current changes slope at a low temperature (at about $T < 90$ K). The reduction in the dark current slope at low temperatures may be explained by the fact that the electrons in the InP layer do not gain enough thermal energy for thermionic emission.

B. Optical gain model

Photon absorption results in the generation of electron–hole pair in the InGaAs absorber. Under a forward bias, the electrons and the holes are separated, and the holes get trapped in the GaAsSb trapping layer for the period of their lifetimes. This leads to a change of barrier potential, and results in a large electron injection, and hence an internal amplification in the device.

The optical gain model for the electron-injection detectors is derived in Ref. 14. The optical gain reduces at high optical power levels. This phenomenon has not

been considered in Ref. 14. We address this issue by attributing this phenomena to the high-level injection effect in the GaAsSb layer and modelling it by introducing an ideality factor $\eta_F(P)$, that depends on power (P), then

$$G_{opt}(P) = \frac{G_{Max} \left[e^{\frac{qV_{BE}(P)}{\eta_F(P)k_BT}} - 1 \right]}{\left[e^{\frac{qV_{BE}(P)}{\eta_F(P)k_BT}} - 1 \right] + G_{Max} \frac{J_{SE}}{J_S} \frac{A_1}{A_2} \left[e^{\frac{qV_{BE}(P)}{\eta_E k_BT}} - 1 \right]}. \quad (17)$$

In (17), J_{SE}/J_S demonstrates the ratio of saturation current density for recombination in the injector/trapping layer space charge region to saturation current density injected into the absorber, A_1/A_2 demonstrates the ratio of injector to absorber area, and G_{Max} is the maximum optical gain. Figure 3(a) shows the Gummel plot for this device, i.e., plot of current under illumination, referred to as the optical current (i_{opt}), versus optical power (P). At low optical power level ($\lesssim 10$ pW), the optical current is limited by dark current. In the low-level injection region, the optical current increases as the optical power is increased. In this region, an ideality factor is $\eta_F \sim 1$. To the right of that region, the optical current
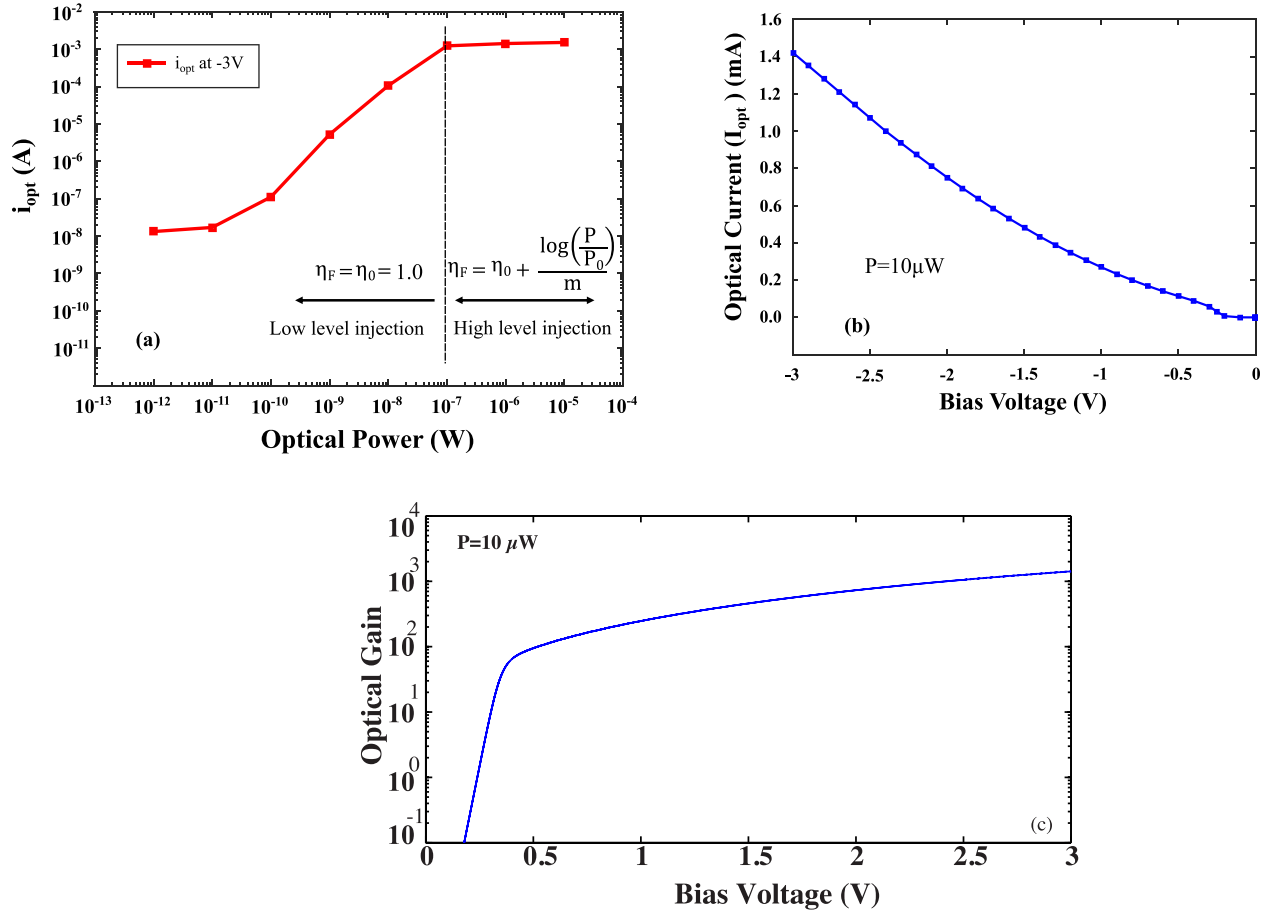
FIG. 3. (a) Optical current versus optical power for the electron-injection detector with $10\,\mu m$ injector size. External Quantum efficiency in our commercial simulator (ATLAS from Silvaco International) is taken as 95%. (b) The optical current versus bias voltage at $10\,\mu$W optical power. (c) Optical Gain versus bias at $10\,\mu$W optical power.

becomes limited by high-level injection effects and the ideality factor increases at high optical power levels. Dependence of the ideality factor to the optical power can be modeled as:

$$: \eta_F(P) = \begin{cases} \eta_0 = 1.0 & P < P_0 \\ \eta_0 + \dfrac{\log\left(\dfrac{P}{P_0}\right)}{m} & P > P_0, \end{cases} \qquad (18)$$

where $P_0 = 10^{-7}$ W, and m is a fitting parameter. For the electron-injection detector with $10\,\mu m$ injector size, $m = 4.0$ provides a good fit.

The optical current versus bias voltage at $10\,\mu$W optical power is shown in Fig. 3(b). As illustrated in the plot of Figure 3(c), the optical gain of the electron-injection detector shows a relatively stable behavior with respect to bias, beyond a bias voltage of ~ -1 V. As a result, when utilized in large format Focal Plane Arrays (FPAs), the electron-injection detector gain does not vary much by the possible voltage and process variations across the FPA.

C. Rise time model

In this section, we derive the differential equation, which governs charging of the device. Our approach here is similar to that in Ref. 17. Figure 4 shows the equivalent circuit for the electron-injection detector.

To analyze the detector response, we assume that the trapping layer (GaAsSb) current consists of a transient photogenerated current source (i_{gen}), which provides transient charges, and a dc internal dark current source I_{dark}. We use a charge control approach given by

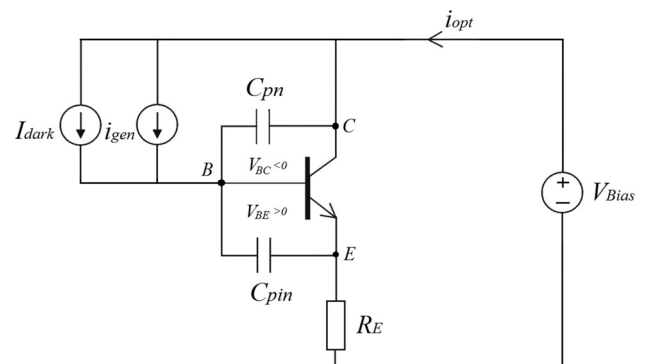$$I_{dark} + i_{gen} = \frac{dQ}{dt} + \frac{Q}{\tau_e} + \frac{dQ_{cap}}{dt}, \qquad (19)$$

FIG. 4. Electron-injection detector equivalent circuit showing the optical current (i_{opt}), photogenerated current source (i_{gen}), internal dark current source (I_{dark}), the junction capacitances (C_{pin}) and (C_{pn}), and the bias voltage source (V_{Bias}).

where Q is the excess minority carrier charge in the GaAsSb region, Q_{cap} is the charge stored at the edges of the junction depletion capacitances, and τ_e is the minority electron life time in the GaAsSb region. The average excess electron spends a time τ_B defined as the transit time from the injector to the absorber. Since the GaAsSb width is made small compared with electron diffusion length, this transit time is much less than the average electron lifetime in the trapping layer. On the other hand, an average excess hole supplied from the InGaAs absorber spends τ_e in the trapping layer facilitating a space charge neutrality during the lifetime of an average excess electron. For each hole entering GaAsSb, τ_e/τ_B electrons should pass from injector to absorber to maintain space charge neutrality.

The first term on the right-hand side of Eq. (19) describes the charging or discharging of the excess charge in the GaAsSb. The second term describes the recombination in the GaAsSb layer. The third term is the current associated with charging or discharging the junction capacitances and supplying the charge to maintain current flow in the space charge region of InGaAs absorption layer. The excess electron charge in the GaAsSb is given by

$$Q = \tau_B i_{opt}, \qquad (20)$$

where τ_B is the GaAsSb transit time, and i_{opt} is the optical current, described in Sec. II B. We assume that the voltage source V_{Bias} is a short circuit to ac signals. Summing the voltages around the injector-absorber circuit in Figure 4, gives the charge stored at the edge of the depletion regions

$$Q_{cap}(t) = |V_{BE}(t)|C_T + i_{opt}(t)R_E C_{pn} + \frac{\tau_{ce} i_{opt}(t)}{2}, \qquad (21)$$

where C_T is the sum of the junction capacitance in the InP/InAlAs/GaAsSb (C_{pin}) and the junction capacitance in the GaAsSb/InGaAs (C_{pn}) layers ($C_T = C_{pin} + C_{pn}$), R_E is the injector resistance, τ_{ce} is the electron transit time in the absorber layer (InGaAs), and $Q_{cap}(t)$, $i_{opt}(t)$, $V_{BE}(t)$ are the time–varying quantities due to the photocurrent. To preserve charge neutrality in the depletion region, a positive charge that is equal in magnitude to the total transiting electron charge is supplied to the edges of region.[17] Under a low-level injection, one can assume that the positive charge is distributed equally between either side of the space charge region between the GaAsSb side and the InGaAs region. The last term in (21) is quasi-static approximation and illustrates the fact that the positive charge, which must be supplied to the GaAsSb side of the GaAsSb/InGaAs space charge region, is half of the negative charge transiting through the space charge region.[17] Using the chain rule and the diode equation, we find that

$$\frac{dV_{BE}}{dt} = \frac{dV_{BE}}{di_{opt}}\frac{di_{opt}}{dt} = \frac{k_B T}{q(i_{opt}+I_S)}\frac{di_{opt}}{dt}, \qquad (22)$$

where I_S is the saturation current. Substituting (20)–(22) into (19) gives

$$I_{dark} + i_{gen} = \tau_B \frac{di_{opt}}{dt} + \frac{\tau_B}{\tau_e}i_{opt} + \frac{k_B T}{q(i_{opt}+I_S)}C_T\frac{di_{opt}}{dt}$$
$$+ R_E C_{pn}\frac{di_{opt}}{dt} + \frac{\tau_{ce}}{2}\frac{di_{opt}}{dt}. \qquad (23)$$

By simplifying Equation (23) and substantiating $\frac{\tau_e}{\tau_B} = G_{opt}$ in (23), we obtain

$$\frac{di_{opt}}{dt} = \frac{G_{opt}(I_{dark}+i_{gen}) - i_{opt}}{\tau_e + G_{opt}R_E C_{pn} + G_{opt}\dfrac{k_B T}{q(i_{opt}+I_S)}C_T + \dfrac{G_{opt}\tau_{ce}}{2}}. \qquad (24)$$

As shown in Figure 3, optical current (i_{opt}) in the dark has a value of $G_{opt}I_{dark}$. Here we assume that the internal dark current, I_{dark} is such that the optical current will always be much greater than the saturation current, i.e., $i_{opt(min)} = G_{opt} I_{dark} \gg I_S$. The rise time defined as the time elapsed for the output current to change from 10% to 90% of its maximum, as a result of an applied rectangular input light pulse, otherwise called "charge–up time" can be found by integrating both sides of Equation (24). The lower and upper limits of integration are taken as $G_{opt}(I_{dark} + 0.1 i_{gen})$ and $G_{opt}(I_{dark} + 0.9 i_{gen})$, respectively, and i_{gen} is assumed to be a constant. Assuming that $G_{opt} + 1 \approx G_{opt}$, the rise time is given by

$$t_{Rise} = 2.2\left(\tau_e + G_{opt}R_E C_{pn} + \frac{G_{opt}\tau_{ce}}{2}\right)$$
$$+ \left(2.2 + \ln\left\{\frac{I_{dark}+0.9 i_{gen}}{I_{dark}+0.1 i_{gen}}\right\}\right)\frac{k_B T}{q(I_{dark}+i_{gen})}C_T. \qquad (25)$$

In this model, i_{opt}, and G_{opt} are optical power dependent quantities and can be obtained from Equation (17). I_{dark} can be found from Equations (10), (16), and (17). C_{pn} and C_T are taken as fitting parameters, which are in good agreement with our calculations. R_E is the dynamic resistance calculated from $\frac{0.0025*m}{I_{dark}+I_{opt}}$. Parameter values required to calculate the rise time from Equation (25) are provided in Table II. To obtain the rise time of the detector, from the implemented structure in the numerical simulator, a pulsed monochromatic collimated source at 1550 nm wavelength was used.

III. DISCUSSION AND RESULTS

To provide useful information and guidelines for the development of optimized electron-injection detectors as well as other heterojunction photodetectors, in this section, we evaluate the effect of variation in key detector parameters on its electrical and optical characteristics. These parameters include the thicknesses of GaAsSb trapping layer and the InAlAs etch-stop layers, as well as the doping concentrations of the InP injector and the GaAsSb trapping layer. Effect of geometry has been previously investigated in Ref. 15. All parameter variation data are taken at a device operating bias of −3 V, and for a device with 10 μm injector and 30 μm absorber, at room temperature. To compare the performance

TABLE II. Parameters used in the analytical model for rise time at room temperature.

Parameter	Symbol	Value	Reference
Transit time in GaAsSb	τ_b	3.5×10^{-13} s	Calculated from base transit time formula using electron diffusion coefficient in GaAsSb of 50 cm²/s from Ref. 23
Transit time in InGaAs	τ_{ce}	1×10^{-12} s	Calculated from collector transit time formula using velocity saturation for InGaAs 2.8×10^7 cm/s.[23]
$C_{pin} + C_{pn}$	C_T	5×10^{-13} F	Fitting
Junction capacitance in GaAsSb/InGaAs	C_{pn}	1×10^{-14} F	Fitting

of devices with different thicknesses and doping concentrations, we propose a figure of merit (FOM) as

$$FOM = \frac{NEP}{\sqrt{BW}}. \qquad (26)$$

The most commonly used figure of merit for photon detectors is the noise-equivalent-power (NEP).[20] Noise-equivalent-power is extremely useful for optical power measurements. However, it does not take into account the timing performance of the photon detector. As such, to take into account the bandwidth (BW), we defined a new FOM, which essentially gives the minimum energy that can be sensed by the detector and has a minimum of 1.2×10^{-19} J, which is the energy of one photon at 1550 nm wavelength. In Equation (26), $BW = 0.35/t_{Rise}$, and NEP is obtained by dividing the

noise current, $I_n = \sqrt{2Fq < i_{dark} > G_{opt}}$, by responsivity (given by: $R = (i_{opt} - i_{dark})/P$).[18] Excess noise factor is taken as unity and has been experimentally verified in Ref. 13. In each of Secs. III A–III D, only the parameter under investigation has been varied, and all other parameters are kept the same as in the original structure provided in Section I. The study provided in this section suggests that an optimized EI structure would yield at least 20% performance improvement compared to our existing (original) structure, which was introduced in Section I.

A. The Effect of variation in GaAsSb thickness

In our simulation and theoretical models, the GaAsSb layer thickness was reduced from 50 nm (in the original structure) to 10 nm. Figure 5(a) shows the effect of variation
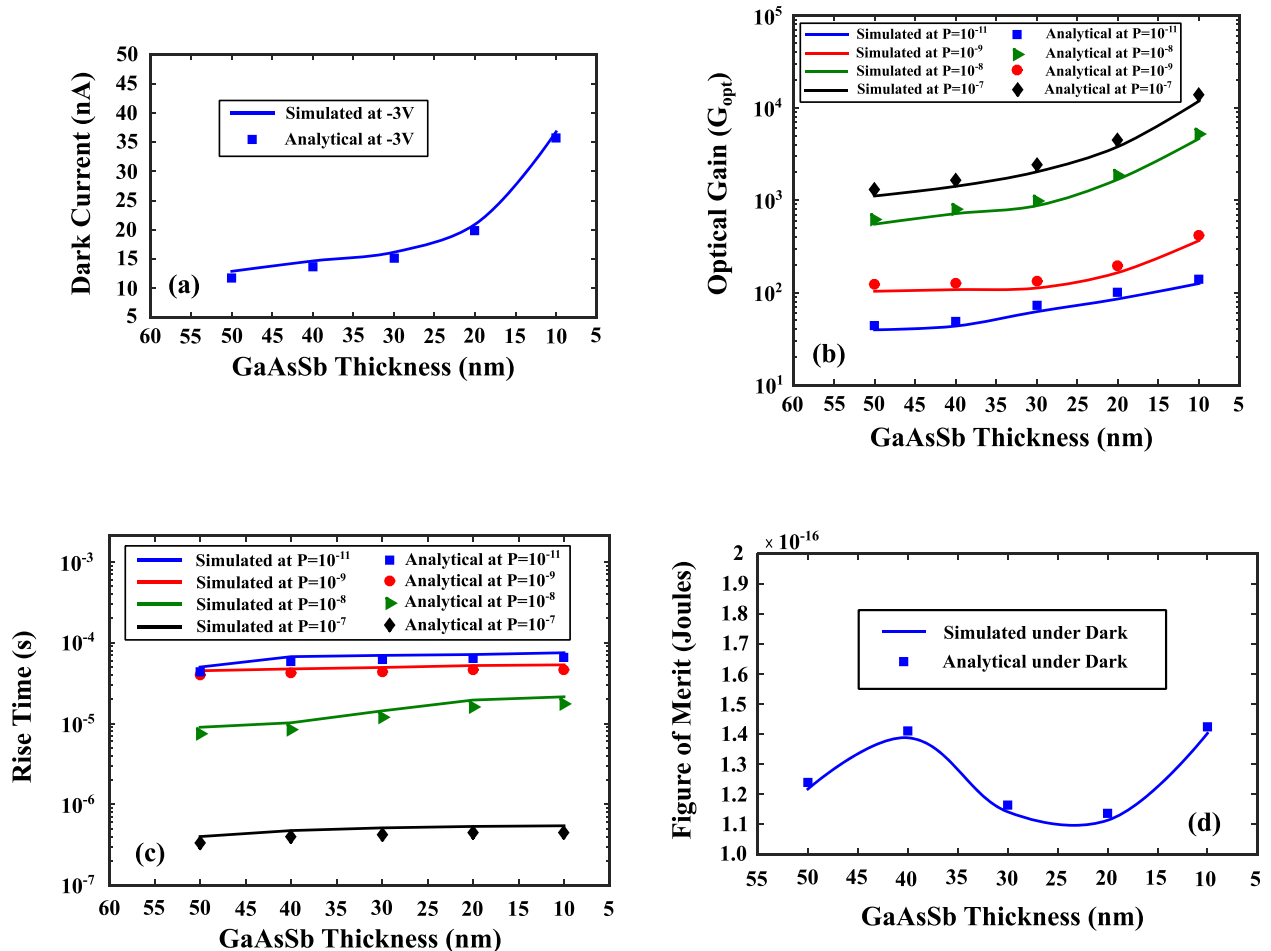

FIG. 5. Modeling results showing detector (a) dark current (b) optical gain (c) rise time, and (d) figure of merit as a result of variations in GaAsSb thicknesses.

in GaAsSb thickness on the dark current. Our models predict that a device with 10 nm trapping layer thickness exhibits the dark current about 36 nA at -3 V bias voltage. Figure 5(b) shows the optical gain at different optical power levels. For 10 nm trapping layer thickness, optical gains as high as 12000 can be achieved. Figure 5(c) shows the rise time versus GaAsSb thickness at different optical power levels. Variation in the trapping layer thickness from 10 nm to 50 nm, hardly affects the device rise time. Variation of the FOM is shown in Figure 5(d) for different GaAsSb thicknesses. The modeling results predict that an improvement of 10% in our current device performance (with 50 nm GaAsSb thickness) is expected by reducing the GaAsSb thickness to $\sim$25 nm. At a GaAsSb layer thickness of 10 nm, and a temperature of $\sim$79 K, our models suggest a FOM of 1.23×10^{-19} can be achieved corresponding to the energy of 1 photon at 1550 nm.

B. The effect of variation in InAlAs thickness

The effect of variation in the InAlAs layer thickness on the device performance is explored in this. Figure 6(a) shows the effect of variation in InAlAs layer thickness on the dark current. Our modeling results predict that a device with 10 nm InAlAs etch-stop layer thickness exhibits the dark current about 338 nA at -3 V bias voltage. Figure 6(b) shows the optical gain at different optical power levels. One of the major shortcomings of the existing electron-injection detector structures is that their

gain drops to half of its peak value at the photo generated current density of 10^{-4} A cm^{-2}.[14,15] This prevents their utilization in experiments that require the detection of few photons, when the electrical noise from the amplifier dominates.[18] Our models suggest that reducing the InAlAs layer thickness could address this major challenge in the detector operation at a low power regime. For the device with 10 nm InAlAs thickness, the optical gain as high as 1000 can be achieved at low optical power levels ($\sim$100 pW). Figure 6(c) shows the rise time versus InAlAs thickness at different optical power levels. Reduction of the InAlAs thickness, decreases the rise time due to an increase in the electric field in the InAlAs region. Variation in the figure of merit is shown in Figure 6(d) for different InAlAs thickness. The simulation results predict that the electron-injection detector with 10 nm etch-stop thickness has a FOM about 1.2×10^{-16} J. This is equivalent to sensing $\sim$1000 photons (at 1550 nm wavelength) at room temperature. Furthermore, at a temperature of 75 K, our models suggest that a FOM of 1.32×10^{-19} can be achieved for a detector with 10 nm InAlAs thickness corresponding to the energy of 1 photon at 1550 nm.

C. The Effect of variation in injector (InP) doping

Figure 7(a) shows the dark current versus injector doping concentration. As the injector doping is increased, the dark current is also increased. The dark current increases from 15 nA at $N_D = 10^{17}$ cm^{-3} (original structure) to 160 nA
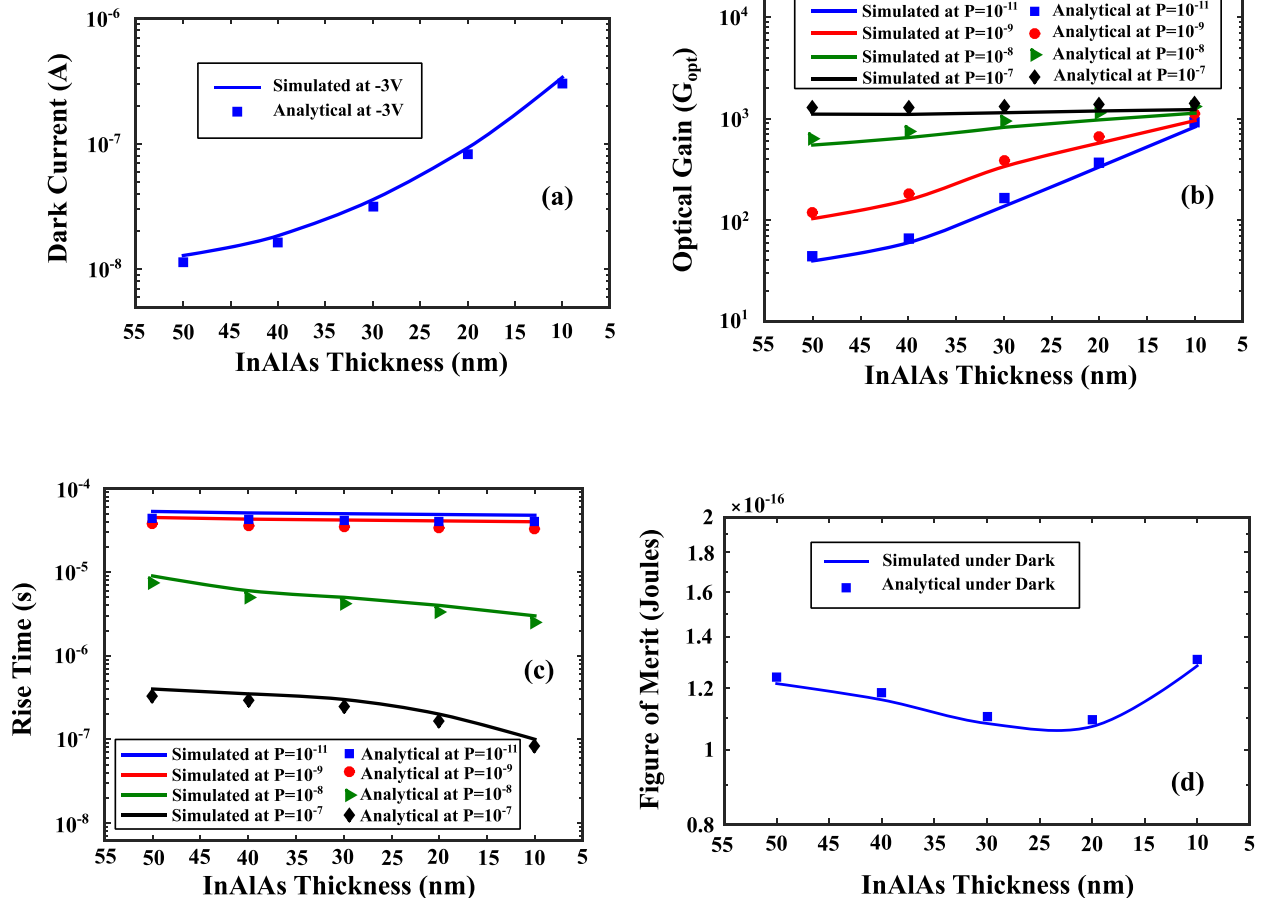

FIG. 6. Modeling results showing detector (a) dark current (b) optical gain (c) rise time, and (d) figure of merit as a result of variations in InAlAs thicknesses.
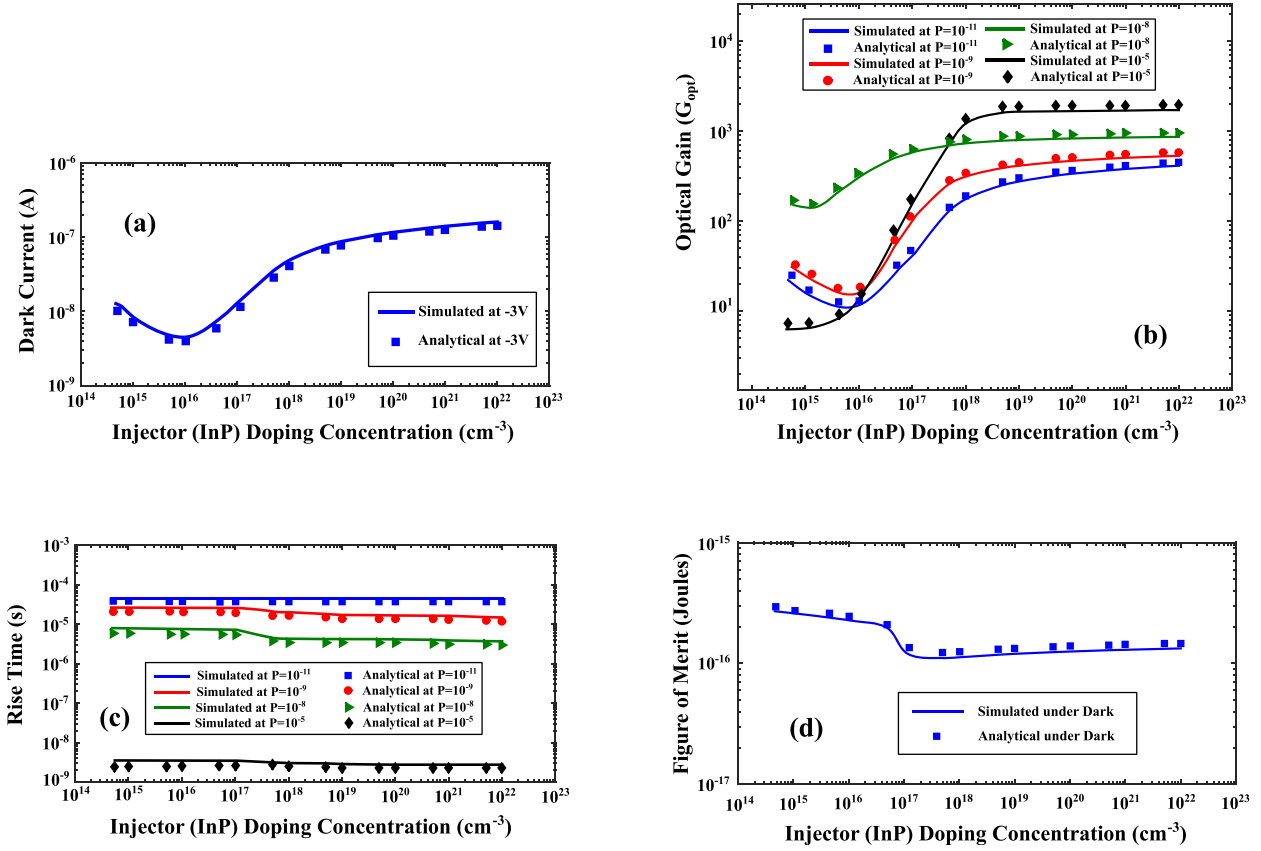
FIG. 7. Modeling results showing detector (a) dark current (b) optical gain (c) rise time, and (d) figure of merit as a result of variations in InP doping concentration.

at $N_D \sim 10^{19} \text{cm}^{-3}$. This is consistent with our simulation model, which shows that as InP doping concentration is increased, the injected electron concentration into the absorption region is increased, and E_{Fn} is increased. As the carrier concentration in the injector reduces, the injector depletion layer width increases. This leads to an increase in the dark current, since at the same time, diffusion current is reduced and generation current is increased. Figure 7(b) shows the effect of variation in the injector impurity concentration on the optical gain calculated for various optical power levels. The optical gain increases from 40 at $N_D = 10^{17} \text{cm}^{-3}$ to 411 at $N_D \sim 10^{18} \text{cm}^{-3}$ at low optical power levels. Increasing doping concentration beyond $N_D = 10^{18} \text{cm}^{-3}$ does not significantly increase the gain. Degeneracy is typically caused by heavy doping, with N_D in excess of approximately 2.84 $\times 10^{16} \text{cm}^{-3}$ in InP at room temperature.[21] The effect of variations in injector doping concentration on the rise time is depicted in Figure 7(c) for various optical power levels. Figure 7(d) shows that the minimum FOM is obtained for an InP concentration of $\sim 10^{18} \text{cm}^{-3}$. As shown in Figure 7(d), the modeling results predict that an improvement of 10% in our current device performance (with an InP doping concentration of $\sim 10^{17} \text{cm}^{-3}$) is expected by increasing InP doping to $\sim 10^{18} \text{cm}^{-3}$, where a minimum of FOM is obtained.

D. The effect of variations in GaAsSb doping

The effect of GaAsSb layer doping concentration is examined in this section. The variation of dark current versus

GaAsSb doping concentration is shown in Figure 8(a). As the carrier concentration in the trapping layer (GaAsSb) reduces, the depletion layer widths x_{p1} and x_{p2} increase. This leads to an increase in the dark current, since at the same time generation, current is increased. As the GaAsSb impurity concentration is increased, the dark current reduces dramatically from $1.0 \times 10^{-3} \text{A}$ at $N_A = 10^{15} \text{cm}^{-3}$ to $7.66 \times 10^{-10} \text{A}$ at $N_A = 10^{20} \text{cm}^{-3}$ due to an increase in potential barrier at the interface of InAlAs/GaAsSb layer. The barrier potential increases by 3.107 eV by increasing NA from $N_A = 10^{15} \text{cm}^{-3}$ to $N_A = 10^{20} \text{cm}^{-3}$. Our simulation model shows that electron concentration decreases for the same bias voltage. Figure 8(b) is the optical gain for variations in GaAsSb doping concentrations calculated at difference optical power levels. The variation of rise time versus GaAsSb doping concentration for various optical power is depicted in Figure 8(c). As the GaAsSb doping concentration is increased, the rise time increases, possibly due to increase of junction capacitance (C_{pn} and C_{pin}) and reduction of the dark current. Finally, the figure of merit evaluated for various GaAsSb doping concentrations is shown in Figure 8(d). The minimum is obtained at a GaAsSb doping of 10^{19}cm^{-3}. Degeneracy is typically caused by heavy doping, with N_A in excess of approximately $1.14 \times 10^{20} \text{cm}^{-3}$ in GaAsSb at room temperature.[21]

IV. CONCLUSION

Optimal design of optoelectronic devices requires physically based device models that describe the device characteristics
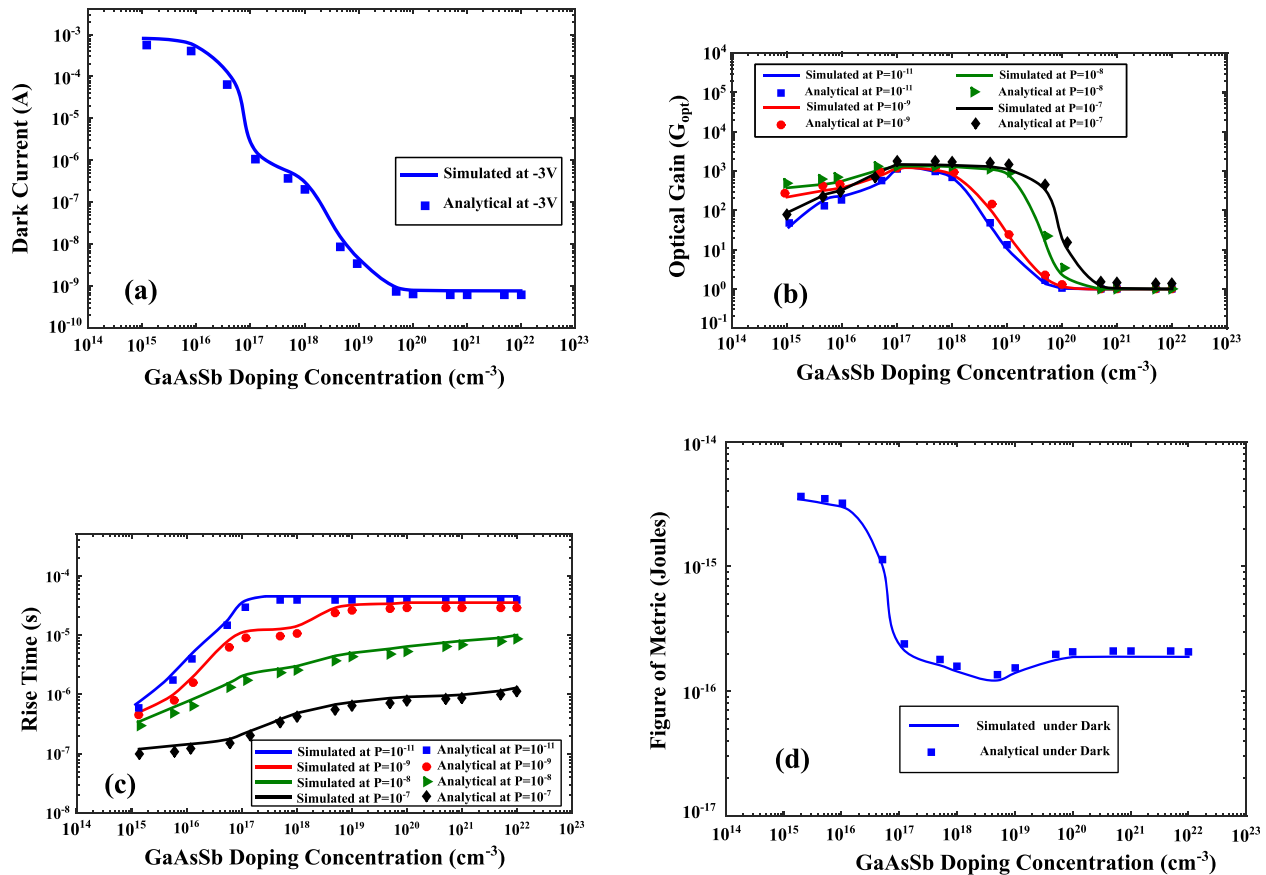
FIG. 8. Modeling results showing detector (a) dark current (b) optical gain (c) rise time, and (d) figure of merit as a result of variations in GaAsSb doping concentration.

accurately. Here we provide analytical models for the electron-injection detector, which are also useful for other heterojunction phototransistors. Models for dark current, rise time, and the optical gain are derived, which allow an easy evaluation of the role of different parameters on key performance characteristics of the device. Our models show that our original device layer structure is very close to the optimum design, and the above optimizations can improve device performance by a further 20%. These results can be a huge improvement for other design structures and provide guidelines for optimization of similar detectors such as phototransistors. Device analysis reveals that increasing the injector doping, decreasing GaAsSb thickness, and reducing InAlAs thickness can all address the major limitation in the electron-injection detector operation, that is, the drop in the gain at low optical powers. For example, reducing the InAlAs layer thickness to 10 nm may result in maintaining the gain at about 1000 at very low-light-level conditions and open up applications for utilization of this device in single photon measurements. According to the simulation and modeling results, the optimized electron-injection detector has a minimum sensitivity of $\sim 10^{-16}$ J at room temperature.

ACKNOWLEDGMENTS

[1]R. M. Marino, W. R. Davis, G. C. Rich, J. L. Mclauling, E. l. Lee, B. M. Stanley, J. W. Burnside, G. S. Rowe, R. E. Hatch, T. E. Square, L. J. Skelly, M. O'Brien, A. Vasile, and R. M. Heinrichs, "High-resolution 3D imaging laser radar flight test experiments," Proc. SPIE **5791**, 138–151 (2005).

[2]E. Knill, R. Laflamme, and G. J. Milburn, "A scheme for efficient quantum computation with linear optics," Nature **409**, 46–52 (2001).

[3]E. Diamanti, C. Langrock, M. M. Fejer, Y. Yamamoto, and H. Takesue, "1.5 μm photon-counting optical time-domain reflectometry with a single photon detector based on upconversion in a periodically poled lithium niobate waveguide," Opt. Lett. **31**, 727–729 (2006).

[4]A. Poloczek, M. Weiss, S. Fedderwitz, A. Stoehr, W. Prost, D. Jaeger, and F. J. Tegude, "Integrated InGaAs pin-diode on exactly oriented silicon (001) substrate suitable for 10 Gbit/s digital applications," in *Proceedings of 20th Annual Meeting IEEE Lasers and Electro-Optics Society, LEOS* (2007), pp. 180–181.

[5]S. Cova, M. Ghioni, A. Lotito, I. Rech, and F. Zappa, "Evolution and prospects for single-photon avalanche diodes and quenching circuits," J. Mod. Opt. **51**(9/10), 1267–1288 (2004).

[6]N. Duan, S. Wang, X. G. Zheng, X. Li, N. Li, J. C. Campbell, C. Wang, and L. A. Coldren, "Detrimental effect of impact ionization in the absorption region on the frequency response and excess noise performance of InGaAs-InAlAs SACM avalanche photodiodes," IEEE J. Quantum Electron. **41**(4), 568–572 (2005).

[7]R. J. McIntyre, "Multiplication noise in uniform avalanche diodes," IEEE Trans. Electron Devices **ED-13**, 164–168 (1966).

[8]O. G. Memis, A. Katsnelson, S. C. Kong, H. Mohseni, M. Yan, S. Zhang, T. Hossain, N. Jin, and I. Adesida, Appl. Phys. Lett. **91**, 171112 (2007).

[9]V. Fathipour, O. G. Memis, S. J. Jang, F. Khalid, R. Brown, I. Hassani Nia, R. M. Gelfand, and H. Mohseni, "Isolated nano-injection photo detectors for high-speed and high-sensitivity single-photon detection," Proc. SPIE **8868**, 886803 (2013).

[10]V. Fathipour, S. J. Jang, I. Hassani Nia, and H. Mohseni, "Approaching high temperature photon counting with electron-injection detectors," Proc. SPIE Infrared Sens. Device. Appl. IV **9220**, 92200J (2014).

[11]O. G. Memis, A. Katsnelson, S. C. Kong, H. Mohseni, M. Yan, S. Zhang, T. Hossain, N. Jin, and I. Adesida, "Sub-Poissonian shot noise of a high internal gain injection photon detector," Opt. Express **16**(17), 12701 (2008).

[12]V. Fathipour, S. J. Jang, R. Brown, and H. Mohseni, "Highly sensitive and linear electron-injection detectors at the telecom wavelength," in *Frontiers in Optics (FiO), Tucson, Arizona, USA*, 19–23 October 2014.

[13]V. Fathipour, O. G. Memis, S. J. Jang, R. L. Brown, I. Hassani Nia, and H. Mohseni, "Isolated electron injection detectors with high gain and record Low dark current at telecom wavelength," IEEE J. Sel. Top. Quantum Electron. **20**(6), 65 (2014).

[14]V. Fathipour, S. J. Jang, I. Hassani Nia, and H. Mohseni, "Impact of 3D Geometry on performance of electron-injection infrared detectors," Appl. Phys. Lett. **106**(2), 021116 (2015).

[15]Y. Movassaghi, V. Fathipour, M. Fathipour, and H. Mohseni, "Analytical modeling and numerical simulation of the short-wave infrared electron-injection detectors," Appl. Phys. Lett. **108**, 121102 (2016).

[16]P. Chakrabarti, A. Krier, and A. F. Morgan, "Analysis and simulation of a mid-infrared Pþ-InAs0.55Sb0.15P0.30/n0-InAs0.89Sb0.11/ Nþ-InAs0.55Sb0.15P0.30 double heterojunction photodetector grown by LPE," IEEE Trans. Electron Devices **50**, 2049–2058 (2003).

[17]J. P. Helme and P. A. Houston, "Analytical modeling of speed response of heterojunction bipolar phototransistors," J. Lightwave Technol. **25**(5), 1247–1255 (2007).

[18]V. Fathipour, I. H. Nia, A. Bonakdar, and H. Mohseni, "On the Sensitivity of Electron-Injection Detectors at Low Light Level," in IEEE Photonics J. **8**, 1–7 (2016).

[19]R. S. Muller and T. I. Kamins, *Device Electronics for Integrated Circuits*, 3rd ed. (Wiley, 2002).

[20]S. Donati, *Photodetectors: Devices, Circuits and Applications* (Prentice Hall, 2000), Chap. 3.

[21]R. F. Pierret, *Advanced Semiconductor Fundamental* (Addison-Wesley Publishing Company, 1987).

[22]S. M. Sze and K. K. Ng, *Physics of Semiconductor Devices* (John Wiley & Sons, 2006).

[23]See http://www.ioffe.ru/SVA/NSM/semicond/ for the experimental parameters used in Table I.

[24]I. Vurgaftman, J. R. Meyer, and L. R. Ram-Mohan, "Band parameters for III–V compound semiconductors and their alloys," J. Appl. Phys. **89**(11), 5815–5875 (2001).

[25]S. Datta, S. Shi, K. P. Roenker, M. M. Cahay, and W. E. Stanchina, "Simulation and design of InAlAs/InGaAs pnp heterojunction bipolar transistors," IEEE Trans. Electron Devices **45**(8), 1634–1643 (1998).